PHYSICAL REVIEW C **80**, 044614 (2009)

Effect of repulsive and attractive three-body forces on nucleus-nucleus elastic scattering

T. Furumoto*
Department of Physics, Osaka City University, Osaka 558-8585, Japan

Y. Sakuragi†
Department of Physics, Osaka City University, Osaka 558-8585, Japan and
RIKEN Nishina Center, RIKEN, Wako, Saitama 351-0198, Japan

Y. Yamamoto‡
Physics Section, Tsuru University, Tsuru, Yamanashi 402-8555, Japan

(Received 8 June 2009; revised manuscript received 12 August 2009; published 26 October 2009)

The effect of the three-body force (TBF) is studied in nucleus-nucleus elastic scattering on the basis of Brueckner theory for nucleon-nucleon (NN) effective interaction (complex G matrix) in the nuclear matter. A new G matrix called CEG07 proposed recently by the present authors includes the TBF effect and reproduces a realistic saturation curve in the nuclear matter, and it is shown to well reproduce proton-nucleus elastic scattering. The microscopic optical potential for the nucleus-nucleus system is obtained by folding the G matrix with nucleon density distributions in colliding nuclei. We first analyze in detail the $^{16}\text{O} + ^{16}\text{O}$ elastic scattering at $E/A = 70$ MeV. The observed cross sections are nicely reproduced up to the most backward scattering angles only when the TBF effect is included. The use of the frozen-density approximation (FDA) is essentially important to properly estimate the effect of the TBF in nucleus-nucleus scattering. Other prescriptions for defining the local density have also been tested, but only the FDA prescription gives a proper description of the experimental cross sections as well as the effect of the TBF. The effects of the three-body attraction and the ω-rearrangement term are also analyzed. The CEG07 interaction is compared with CDM3Y6, which is a reliable and successful effective density-dependent NN interaction used in the double-folding model. The CEG07 G matrix is also tested in the elastic scattering of ^{16}O by the ^{12}C, ^{28}Si, and ^{40}Ca targets at $E/A = 93.9$ MeV, and in the elastic scattering of ^{12}C by the ^{12}C target at $E/A = 135$ MeV with great success. The decisive effect of the TBF is clearly seen also in those systems. Finally, we have tested CEG07a, CEG07b, and CEG07c for the $^{16}\text{O} + ^{16}\text{O}$ system at various energies.

DOI: 10.1103/PhysRevC.80.044614 PACS number(s): 21.30.−x, 21.65.−f, 24.10.Ht, 25.70.Bc

I. INTRODUCTION

The role of the nuclear three-body force (TBF) in complex nuclear systems is one of the key issues not only in nuclear physics but also in nuclear astrophysics relevant to high-density nuclear matter in neutron stars and supernova explosions. It is well known that the empirical saturation point of nuclear matter (the binding energy per nucleon $E/A \approx 16$ MeV at a saturation density $\rho_0 \approx 0.17$ fm^{-3}) cannot be reproduced by using only two-body nucleon-nucleon (NN) interactions [1]. To obtain a reasonable saturation curve, it is indispensable to take into account the additional contributions of the TBF, which contains two parts: a three-body attraction (TBA) and a three-body repulsion (TBR). It is important here that the saturation curve in the high-density region is strongly pushed upward by the TBR contribution, and, as the result, the nuclear-matter incompressibility becomes large [2–5]. This effect is intimately related to our problem. In Ref. [6], we reported for the first time clear evidence of the important role of the TBF (especially the TBR) in nucleus-nucleus elastic scattering in the case of an $^{16}\text{O} + ^{16}\text{O}$ system at $E/A = 70$ MeV.

Understanding nucleon-nucleus (NA) and nucleus-nucleus (AA) interactions microscopically starting from underlying NN interactions has been a longstanding and fundamental subject. To solve a complicated many-body problem in nuclear reactions, one needs to rely upon a realistic approach based on reasonable approximations. One of the promising approaches would be to derive the NA and AA folding potentials on the basis of the lowest order Brueckner theory. Here, the NNG-matrix interactions are obtained in infinite nuclear matter and folded into NA and AA density distributions with the local-density approximation (LDA). The Bethe-Goldstone (B-G) equation is solved for an NN pair in medium, one of which corresponds to an incident nucleon and the other is under a scattering boundary condition. The obtained G-matrix interaction is composed of real and imaginary parts, being dependent on the incident energy and the nuclear-matter density. As noted here, the G matrix is considered to be an effective NN interaction in nuclear medium, into which the short-range and tensor correlations are renormalized.

The folding-model study with the use of complex G-matrix interactions for the NA system has a long history. Various G-matrix interactions starting from different kinds of free-space NN interactions were proposed and applied to the analysis of proton-nucleus elastic scattering with more or less successful results. However, all of the G matrices proposed so far were derived from just the two-body force, and the effect

---

*furumoto@ocunp.hep.osaka-cu.ac.jp
†sakuragi@ocunp.hep.osaka-cu.ac.jp
‡yamamoto@tsuru.ac.jp

of the TBF was not included nor discussed. This is partly because the TBF contributions at densities lower than ρ_0 have been considered to be not large enough to affect NA scattering observables. Here, one should note that the local density felt by the incident nucleon inside the target nucleus does not exceed ρ_0 even deep inside the nucleus in usual cases.

Recently, the present authors proposed a new complex G-matrix interaction CEG07 [7] derived from the extended soft-core (ESC) model [8,9]. The ESC model is designed to give a consistent description of interactions not only for the NN system but also for nucleon-hyperon and hyperon-hyperon systems. In this model, the TBR effect is represented as density dependences of two-body parts which appear by changing vector-meson masses in a density-dependent way [9]. In contrast, the TBA part typically results from two-pion exchange with excitation of an intermediate Δ resonance, that is, the Fujita-Miyazawa diagram [10], which gives an important contribution at low densities. Although the saturation curve of nuclear matter can be produced reasonably as combined contributions of the TBA and the TBR, it is decisively important in our results that the TBR contribution becomes more and more significant as the density increases. The CEG07 models were first applied to the analysis of proton-nucleus elastic scattering over a wide range of incident energies and target nuclei with great success [7]. Although the inclusion of the TBF effect, in general, gave rise to only a minor change of pA elastic-scattering cross sections, as expected from our earlier discussion, it was demonstrated that the inclusion of the TBF effect clearly improved the fit to the analyzing power data at forward angles in some energy regions.

In the AA scattering system, the local density $(\rho_1 + \rho_2)$ in the projectile-target overlap region may exceed the normal density of nuclear matter, ρ_0, and could reach about twice this value under the frozen-density approximation (FDA), as mentioned later. The TBR contributions are remarkably large in such high-density regions; hence, one may expect clear evidence of a TBR effect through the calculated folding-model potential (FMP) and the resultant elastic-scattering observables. The importance of a consistent description of nuclear saturation properties and elastic scattering of AA systems was first pointed out by Khoa *et al.* [11,12] on the basis of folding-model analyses. They used density-dependent effective NN interactions such as DDM3Y, BDM3Y, and CDM3Y obtained from the density-independent effective interaction M3Y [13] by multiplying various kinds of phenomenological density-dependent factors by hand, the parameters of which were chosen so as to represent various types of saturation curves in nuclear matter. The real part of the AA potential was calculated by the folding of these interactions with nucleon densities of the AA system, whereas the imaginary part was treated in a completely phenomenological way because M3Y was composed only of a real part. They showed the importance of using an effective interaction to be chosen to reproduce the realistic saturation curve in nuclear matter for the proper description of elastic scattering of AA systems. However, their purely phenomenological density-dependent factor had no explicit or logical relation to the TBF in the nuclear medium.

The present paper is organized as follows. Section II gives the expressions of the G-matrix interaction and the double-folding model for a nucleus-nucleus potential with the use of the complex G-matrix interactions. Our analyses for various scattering AA systems are given in Sec. III. Here, the importance of the TBF effect is demonstrated in the typical case of the $^{16}\mathrm{O} + {}^{16}\mathrm{O}$ elastic scattering at $E/A = 70$ MeV, and then the analyses are performed for the elastic scattering of $^{16}\mathrm{O}$ on the $^{12}\mathrm{C}$, $^{28}\mathrm{Si}$, and $^{40}\mathrm{Ca}$ targets at $E/A = 93.9$ MeV, for the $^{12}\mathrm{C} + {}^{12}\mathrm{C}$ elastic scattering at $E/A = 135$ MeV and for the $^{16}\mathrm{O} + {}^{16}\mathrm{O}$ elastic scattering at various energies. The summary of this work is given in Sec. IV.

II. FORMALISM

A. *G*-matrix interaction

Let us recapture the derivation of the G-matrix interaction given in our previous work [7]. We start from the G-matrix equation for the nucleon pair of the moving nucleon with momentum $\boldsymbol{k}$ and a bound nucleon with momentum $\boldsymbol{k_j}$ in symmetric nuclear matter at the Fermi momentum k_F, where the starting energy ω is given as the sum of the energy $E(k)$ of the propagating nucleon and a single-particle (s.p.) energy $e(k_j)$. The G-matrix calculations are performed with the continuous choice for intermediate nucleon spectra. The scattering boundary condition with $i\varepsilon$ in the denominator leads to complex G matrices, summation of which gives the complex s.p. potential $U(k, E(k))$. Then, the energy $E(k) = \frac{\hbar^2}{2m}k^2 + U_R(k)$ is determined self-consistently, $U_R(k)$ being the real part of $U(k, E(k))$.

Relative and center-of-mass momenta are given as $\boldsymbol{q} = (\boldsymbol{k} - \boldsymbol{k_j})/2$ and $\boldsymbol{P} = \boldsymbol{k} + \boldsymbol{k_j}$, respectively. Angular momenta of relative-orbital, spin, and total states are denoted by L, S, and J, respectively, and isospin is done by T. Then, the coordinate-space G-matrix equation in a (L, S, J, T) pair state is represented as

$$\begin{aligned} u_{LL'}^{JST}(r;q) &= j_L(qr)\delta_{LL'} \\ &\quad + 4\pi\sum_{L''}\int r'^2 dr' F_L(r, r'; q) V_{L'L''}^{JST}(r') u_{LL''}^{JST}(r'; q) \\ F_L(r, r'; q) &= \frac{1}{2\pi^2}\int q'^2 dq' \\ &\quad \times \frac{\bar{Q}(q', \bar{P}; k_F) j_L(q'r) j_L(q'r')}{\omega - \left(\frac{\hbar^2}{m}q'^2 + \frac{\hbar^2}{4m}\bar{P}^2 + U_R(\bar{q}'_+) + U_R(\bar{q}'_-)\right)}, \end{aligned} \tag{1}$$

where $j_L(qr)$ is a spherical Bessel function for the incident momentum q, and $u_{LL'}^{JST}(r;q)$ is the corresponding scattering wave function. $\bar{Q}$, $\bar{P}$, and $\bar{q}'_\pm$ are the angle-averaged expressions for the Pauli operator Q, the center-of-mass momentum P, and $|\boldsymbol{q}' \pm \frac{1}{2}\boldsymbol{P}|$, respectively. The G-matrix elements and the s.p. potentials are given as

$$\langle q|G_{LL}^{JST}|q\rangle = 4\pi\sum_{L''}\int r^2 dr j_L(qr) V_{LL''}^{JST} u_{LL''}^{JST}(r;q), \tag{2}$$

$$U(k, E(k); k_F) = \frac{1}{2\pi^2} \int q^2 dq Z(q; k, k_F) \times \sum_{LJST} \frac{1}{2}(2J+1)(2T+1)\langle q|G_{LL}^{JST}|q\rangle, \tag{3}$$

with

$$Z(q; k, k_F) = \frac{1}{kq}\left(k_F^2 - (k-2q)^2\right). \tag{4}$$

The G-matrix interaction represented as a local form in the coordinate space can be given as

$$G_{LL'}^{JST}(r; k_F, E) = \frac{\int q^2 dq Z(q; k, k_F) j_{L'}(qr) \sum_{L''} V_{L'L''}^{JST}(r) u_{LL''}^{JST}(r; q)}{\int q^2 dq Z(q; k, k_F) j_{L'}(qr) j_L(qr)}, \tag{5}$$

where the q dependence in the G matrix (2) is averaged over so as to reproduce the s.p. potential (3) in the first-order perturbation. The apparent k dependence in the right side is attributed to the E dependence through the relation $E(k) = \frac{\hbar^2}{2m}k^2 + U_R(k)$. The obtained interaction $G_{LL}^{JST}(r)$ is parametrized in a three-range Gaussian form: the outer two ranges are determined by fitting the radial form of $G_{LL}^{JST}(r)$ in long- and intermediate-range regions, and the innermost part is fixed so as to reproduce the $(LSJT)$-state contribution of the s.p. potential U. The central and LS components of the G-matrix interaction in the (LST) state are given by the adequate linear combinations of G_{LL}^{JST} on J. The L dependence is further averaged for each parity state with the statistical weight given by the denominator of Eq. (5). Thus, we obtain the three-Gaussian potential $G_{\pm}^{ST}(r)$, ± being even and odd parities. Our Gaussian-parametrized G-matrix interaction is named CEG07. The detailed form and the parameters are given in the Appendix.

As for the NN interaction model, we adopt the extended soft core (ESC) model [8,9]. Though many NN interaction models have been proposed so far, the recent models reproduce the experimental phase shifts equally well. The G-matrix interactions derived from these models are considered to give rise to similar results for the nucleon-nucleus scattering observables. A reason for adopting ESC here is in the nuclear saturation problem. As is well known, the empirical saturation point can be reproduced with the use of not only the two-body NN interactions but also the three-body force (TBF) composed of the three-body attraction (TBA) and the three-body repulsion (TBR). The TBA is typically due to the two-pion exchange with excitation of an intermediate Δ resonance, which is the Fujita-Miyazawa diagram. We derive the effective two-body interaction from the TBA, which is added on our G-matrix interaction, according to the formalism in Ref. [14]. In our calculations, the pionic form-factor mass is taken as 420 MeV and the NN correlation effect for the TBA is neglected. On the other hand, the origin of the TBR is not necessarily established. In the ESC approach, the TBR effect is included rather phenomenologically by changing the vector-meson masses M_V in the nuclear matter according to $M_V(\rho) = M_V \exp(-\alpha_V \rho)$ with the parameter α_V, which leads to an effective density-dependent two-body interaction. In this work, we take the two values of $\alpha_V = 0.11$ and 0.18. Now, we obtain the saturation curves in the following three cases: (a) with the two-body interaction only, (b) with TBA and TBR ($\alpha_V = 0.18$), and (c) with TBA and TBF ($\alpha_V = 0.11$).

In cases (a), (b), and (c), the minimum values of saturation curves are −17.8, −14.5, and −16.4 MeV, respectively, at $k_F = 1.53, 1.33,$ and 1.41 fm^{-1}. Correspondingly, the calculated values of the incompressibility K at the normal density are obtained as 106, 259, and 179 MeV, respectively. As shown later, in case (c), we further add a repulsion given by the ω-rearrangement effect, which can be taken into account by using the renormalized s.p. potential $\tilde{U}(k, E(k); k_F) = (1 - \bar{\mathcal{K}})U(k, E(k); k_F)$ instead of $U(k, E(k); k_F)$. Here, $\bar{\mathcal{K}}$ is the averaged correlation probability [7]. In cases (a) and (b), the derived CEG interactions were named CEG07a and CEG07b, and the interaction (c) supplemented by the ω-rearrangement effect as CEG07c [7].

B. Folding potential

We construct the nucleus-nucleus optical model potential (OMP) based on the double-folding model (DFM) with the use of the complex G-matrix interaction CEG07. The microscopic nucleus-nucleus potential can be written as a Hartree-Fock type potential:

$$U_F = \sum_{i\in A_1, j\in A_2} [\langle ij|v_D|ij\rangle + \langle ij|v_{\rm EX}|ji\rangle] \tag{6}$$

$$= U_D + U_{\rm EX}, \tag{7}$$

where v_D and $v_{\rm EX}$ are the direct and exchange parts of the complex G-matrix interaction. The exchange part is a nonlocal potential in general. However, by the plane-wave representation for the NN relative motion [15,16], the exchange part can be localized. The direct and exchange parts of the localized potential are then written in the standard form of the DFM potential as

$$U_D(R) = \int \rho_1(\boldsymbol{r}_1)\rho_2(\boldsymbol{r}_2) v_D(s; \rho, E/A) d\boldsymbol{r}_1\, d\boldsymbol{r}_2, \tag{8}$$

where $\boldsymbol{s} = \boldsymbol{r}_2 - \boldsymbol{r}_1 + \boldsymbol{R}$, and

$$U_{\rm EX}(R) = \int \rho_1(\boldsymbol{r}_1, \boldsymbol{r}_1 + \boldsymbol{s})\rho_2(\boldsymbol{r}_2, \boldsymbol{r}_2 - \boldsymbol{s}) v_{\rm EX}(s; \rho, E/A) \times \exp\left[\frac{i\boldsymbol{k}(R)\cdot\boldsymbol{s}}{M}\right] d\boldsymbol{r}_1\, d\boldsymbol{r}_2. \tag{9}$$

Here, $\boldsymbol{k}(R)$ is the local momentum for nucleus-nucleus relative motion defined by

$$k^2(R) = \frac{2mM}{\hbar^2}[E_{\rm c.m.} - {\rm Re}U_F(R) - V_{\rm Coul}(R)], \tag{10}$$

where $M = A_1A_2/(A_1 + A_2)$, $E_{\rm c.m.}$ is the center-of-mass energy, E/A is the incident energy per nucleon, m is the nucleon mass, and $V_{\rm Coul}$ is the Coulomb potential. A_1 and A_2 are the mass numbers of the projectile and target, respectively. The exchange part is calculated self-consistently on the basis of the local energy approximation (LDA) through Eq. (10). Here, the Coulomb potential $V_{\rm Coul}$ is also obtained by folding the NN Coulomb potential with the proton density distributions of the projectile and target nuclei. The density matrix $\rho(\boldsymbol{r},\boldsymbol{r}')$ is approximated in the same manner as in Ref. [17]:

$$\rho(\boldsymbol{r},\boldsymbol{r}') = \frac{3}{k_F^{\rm eff}\cdot s} j_1\left(k_F^{\rm eff}\cdot s\right)\rho\left(\frac{\boldsymbol{r}+\boldsymbol{r}'}{2}\right), \qquad (11)$$

where $k_F^{\rm eff}$ is the effective Fermi momentum [18] defined by

$$k_F^{\rm eff} = \left((3\pi^2\rho)^{2/3} + \frac{5C_s[\nabla\rho^2]}{3\rho^2} + \frac{5\nabla^2\rho}{36\rho}\right)^{1/2}, \qquad (12)$$

where we adopt $C_s = 1/4$ following Ref. [19]. The different value of $C_s = 1/16$ was also suggested [19]. So, we tested the latter value, but no significant difference from the case with $C_s = 1/4$ is observed in the present nucleus-nucleus scattering. The detailed methods for calculating U_D (direct part) and $U_{\rm EX}$ (exchange part) are the same as those given in Refs. [20] and [11], respectively.

In the present calculations, we employ the so-called frozen density approximation (FDA) for evaluating the local density. The prescriptions other than the FDA for evaluating the local density in AA systems are tested in Sec. III A2. In the FDA, the density-dependent NN interaction is assumed to feel the local density defined as the sum of densities of colliding nuclei evaluated at the midpoint of the interacting nucleon pair, that is,

$$\rho = \rho_1\left(\boldsymbol{r}_1 + \tfrac{1}{2}\boldsymbol{s}\right) + \rho_2\left(\boldsymbol{r}_2 - \tfrac{1}{2}\boldsymbol{s}\right). \qquad (13)$$

The FDA has been widely used also in the standard DFM calculations [11,12,19,21,22]. The various prescriptions of the LDA were discussed in Refs. [19,23–25]. We will discuss in more detail in Sec. III A2 how one should define the local density to be used in the LDA for nucleus-nucleus elastic-scattering systems.

III. RESULTS

Let us apply the CEG07 G-matrix interactions to nucleus-nucleus (AA) systems through the double-folding model (DFM). Since the imaginary part of the optical potential for AA systems represents all excurrent flux escaping from an elastic scattering channel through all the possible open reaction channels, it would be difficult to completely simulate those flux losses by the imaginary part of the G-matrix interaction originating from the pair-scattering correlations in the nuclear matter. So, we introduce the renormalization factor N_W phenomenologically for the imaginary part of the FMP and define the present microscopic optical potential with the CEG07 interaction as

$$U_{\rm opt}(R) = V(R) + iN_W W(R). \qquad (14)$$

Here, V and W denote the real and imaginary parts of the original DFM potential derived from the G-matrix interaction. We adjust the renormalization factor so as to attain optimum fits to the experimental data for elastic-scattering cross sections.

First, we analyze elastic scattering of the ^{16}O + ^{16}O system in detail as a benchmark system for testing the interaction model, and then we also analyze the ^{16}O scattering by other target nuclei as well as the ^{12}C + ^{12}C system. We adopt the nucleon density of ^{16}O calculated from the internal wave functions generated by the orthogonal condition model (OCM) by Okabe [26] based on the microscopic α + ^{12}C cluster picture. For other nuclei, we use the nucleon densities deduced from the charge densities [27] extracted from electron-scattering experiments by unfolding the charge form factor of a proton in the standard way [28].

A. ^{16}O + ^{16}O elastic scattering

In this paper, we use the CEG07 G-matrix interactions with and without the TBF effect and analyze the elastic scattering of the ^{16}O + ^{16}O system to see how the TBF effect plays an important role in AA scattering systems. We choose elastic scattering of the ^{16}O + ^{16}O system for the following reasons: ^{16}O is one of the most stable double-magic nuclei and has no collective-excitation state strongly coupled with the ground state. This is important for a folding model based on the complex G matrix, because the imaginary part of the G matrix is expected to simulate the effect of single-particle-like excitations of finite nuclear systems through NN pair-scattering correlations, and the effect of coherent, collective excitations of a finite nucleus may not be included in the imaginary part of the G matrix. Therefore, the ^{16}O + ^{16}O system is an ideal benchmark system for testing the validity of interaction models; in fact, a number of interaction models, either purely phenomenological [29–31] or microscopic in various senses [11,12,21,22], have been tested for decades on this system as a milestone to be cleared.

1. Importance of three-body force

We now analyze the ^{16}O + ^{16}O elastic scattering at $E/A =$ 70 MeV in full detail, paying special attention to the roles of the TBF in AA scattering systems.

Figure 1 shows the real and imaginary parts of the calculated FMP for the ^{16}O + ^{16}O elastic scattering at $E/A = 70$ MeV with the use of three types of CEG07 G-matrix interactions: CEG07a (without the TBF), CEG07b (with the TBF), and CEG07c (with the TBF). Here, we have used the FDA, defined by Eq. (13), to define the local density for evaluating the G matrix in the DFM expressions in Eqs. (8) and (9). Other prescriptions for defining the local density will be discussed in Sec. III A2. The effect of the TBF composed of the TBA and the TBR is clearly seen in the real part of the FMP over the whole range of internuclear distance, while the effect on the imaginary part is rather small except at short distances below 3 fm. The large difference in the real part is found to be mainly due to the effect of the repulsive part of TBF (TBR). Whereas the attractive part of the TBF (TBA) is found to play only a minor role. The minor effect of the TBA will be shown in Sec. III A3. Here, CEG07c includes the repulsive effect of the ω-rearrangement diagram (Fig. 1 in Ref. [32]), which is one of the higher order diagrams in the G-matrix theory. The TBR strength in CEG07c is taken to be weaker than that in CEG07b; CEG07c is designed so that the combined effect of the weaker TBR and the ω-rearrangement contribution is

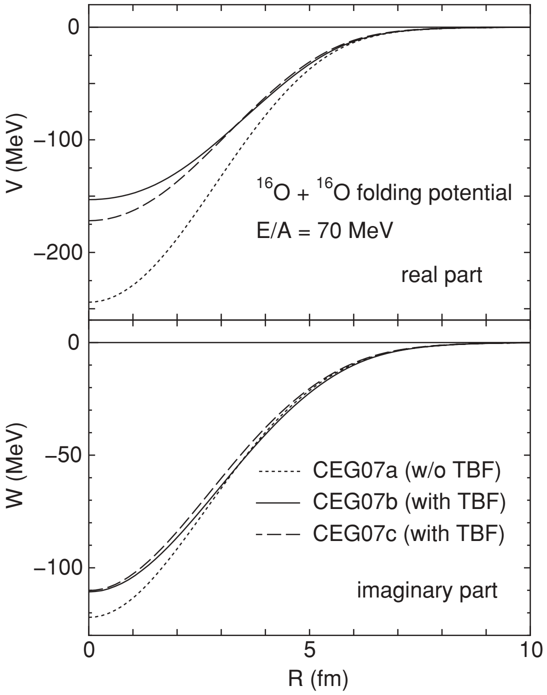

FIG. 1. Real and imaginary parts of the FMP for the $^{16}\mathrm{O} + {}^{16}\mathrm{O}$ system at $E/A = 70$ MeV, obtained with the three types of CEG07 interactions.

similar to the effect of the stronger TBR in CEG07b [7]. The detailed effects of the TBR and ω rearrangement in CEG07c will be discussed in Sec. III A4. The rms radii and the volume integral per nucleon pair of the real and imaginary parts of FMPs calculated with CEG07 are shown in Table I.

TABLE I. The rms radii (R_{rms}) and the volume integral per nucleon pair ($J/A_{\mathrm{P}}A_{\mathrm{T}}$) of the real and imaginary parts of the FMPs calculated with three types of CEG07.

System	E/A (MeV)	CEG07	R_{rms} (fm)		$J/A_{\mathrm{P}}A_{\mathrm{T}}$ (MeV fm^3)	
			Real	Imag.	Real	Imag.
$^{16}\mathrm{O} + {}^{16}\mathrm{O}$	70.0	a	4.242	4.577	−253.0	−140.9
		b	4.409	4.630	−203.6	−142.6
		c	4.335	4.596	−199.9	−132.7
$^{16}\mathrm{O} + {}^{12}\mathrm{C}$	93.9	a	4.150	4.374	−219.0	−143.4
		b	4.376	4.419	−167.2	−146.4
		c	4.271	4.397	−168.9	−135.2
$^{16}\mathrm{O} + {}^{28}\mathrm{Si}$	93.9	a	4.625	4.844	−217.2	−138.6
		b	4.862	4.888	−164.2	−141.8
		c	4.750	4.866	−166.5	−131.1
$^{16}\mathrm{O} + {}^{40}\mathrm{Ca}$	93.9	a	4.891	5.106	−218.0	−137.7
		b	5.129	5.150	−164.7	−141.1
		c	5.017	5.127	−167.0	−130.4
$^{12}\mathrm{C} + {}^{12}\mathrm{C}$	135	a	4.169	4.092	−173.1	−147.3
		b	4.571	4.130	−117.7	−151.5
		c	4.361	4.119	−127.2	−139.0

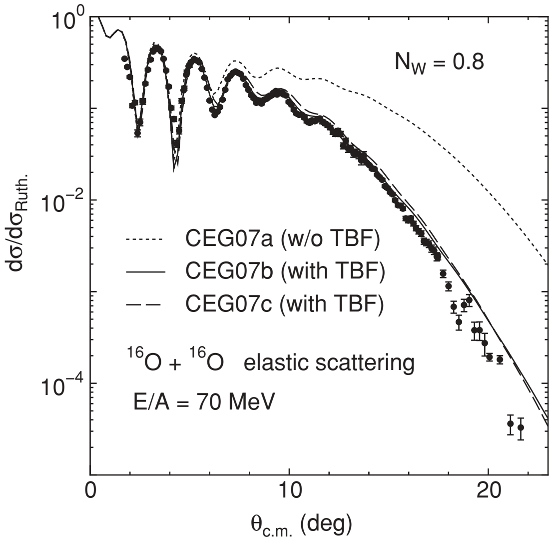

FIG. 2. Rutherford ratio of the cross sections for the $^{16}\mathrm{O} + {}^{16}\mathrm{O}$ elastic scattering at $E/A = 70$ MeV calculated by the FMPs with (CEG07b and CEG07c) and without (CEG07a) the TBF effect, which are compared with the experimental data from Ref. [33]. The N_W value is fixed to 0.8 for all of the calculations.

We then calculate the $^{16}\mathrm{O} + {}^{16}\mathrm{O}$ elastic-scattering cross section at $E/A = 70$ MeV with the use of three types of FMPs shown in Fig. 1. In standard DFM analyses of elastic scattering, it is often the case that the real part of the calculated FMP is multiplied by the renormalization factor, whereas a completely phenomenological imaginary potential is introduced and the parameters together with the renormalization factor for the real FMP are determined so as to optimize the fit to the experimental data. In the present DFM, however, the calculated FMP itself is already complex because of the use of the complex G matrix. The only parameter in the present framework is the renormalization factor N_W for the imaginary part defined by Eq. (14).

The results are shown in Fig. 2. Here, we take N_W to be 0.8, so that the solid curve (with the TBF effect) gives an optimum fit to the data.[1] The solid and dashed curves with the TBF effect well reproduce the experimental data up to backward angles, whereas the dotted curve with CEG07a (without the TBF) overshoots the experimental data at middle and backward angles, reflecting the too deep strength of the real part of the FMP. We found that no reasonable fit to the data was obtained by the FMP with CEG07a (without the TBF) no matter how the imaginary part of the FMP is renormalized by changing the value of N_W, as seen in Fig. 3. When we increase the N_W value so as to reduce the deviation in the large-angle region, no calculation reproduces the proper slope of the experimental cross sections at backward angles, and the diffraction pattern

---

[1] The CEG07 G-matrix interactions used in this work are slightly different from those in Refs. [6,7], because of some improvements for numerical computations and the correction for the minor error found in the G-matrix code. This is the reason why the present value of $N_W = 0.8$ in the $^{16}\mathrm{O} + {}^{16}\mathrm{O}$ scattering at $E/A = 70$ MeV is different from the corresponding one $N_W = 1.0$ in Ref. [6].

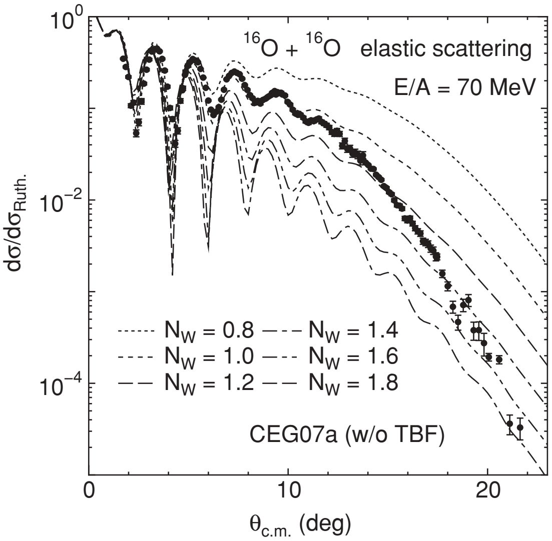

FIG. 3. Same as Fig. 2, but for the results of CEG07a with various renormalization factors for the imaginary part.

in the forward-angle region becomes out of phase with respect to the experimental data. Thus, the large difference between the solid and dotted curves in Fig. 2 clearly shows evidence of the decisive role of the TBF on elastic scattering of the $^{16}\mathrm{O}+{}^{16}\mathrm{O}$ system.

2. *Definitions of local density*

Here, we investigate the definitions of local density and justify the use of the FDA. This is done in the case of the DFM calculation with CEG07b. In the previous section, the importance of the TBF effect has been demonstrated by using the FDA of Eq. (13) to define the local densities in the calculations of the FMPs. In this section, the validity of the FDA is confirmed by the comparison with other prescriptions for defining the local density within the LDA. Let us test the following various definitions of the local density in the calculations of the FMP with CEG07b:

$$\rho = \rho_1 + \rho_2, \tag{15}$$

$$\rho = \frac{1}{2}(\rho_1 + \rho_2), \tag{16}$$

$$\rho = \sqrt{\rho_1 \rho_2}, \tag{17}$$

$$\rho = \begin{cases} \rho_1 + \rho_2 \ldots (\text{if} \quad \rho_1 + \rho_2 < \rho_0), \\ \quad \rho_0 \quad \ldots (\text{if} \quad \rho_1 + \rho_2 > \rho_0), \end{cases} \tag{18}$$

where let us call the definitions given by Eqs. (15) to (18) LDA1 to LDA4, respectively. In Eq. (18), ρ_0 denotes the saturation density in the nuclear matter, that is, $\rho_0 \approx 0.17$ fm^{-3}. LDA1 corresponds to the FDA mentioned before, in which the local density so defined can reach about twice the saturation value $\rho \approx 2\rho_0$ in the largely overlap region, namely, at the short distance between the colliding nuclei. On the other hand, in the other three definitions, LDA2, LDA3, and LDA4, the local density does not exceed the saturation density ρ_0. Let us also call LDA4 the cutting-density approximation (CDA), which modifies the FDA so that ρ does not exceed the saturation value ρ_0.

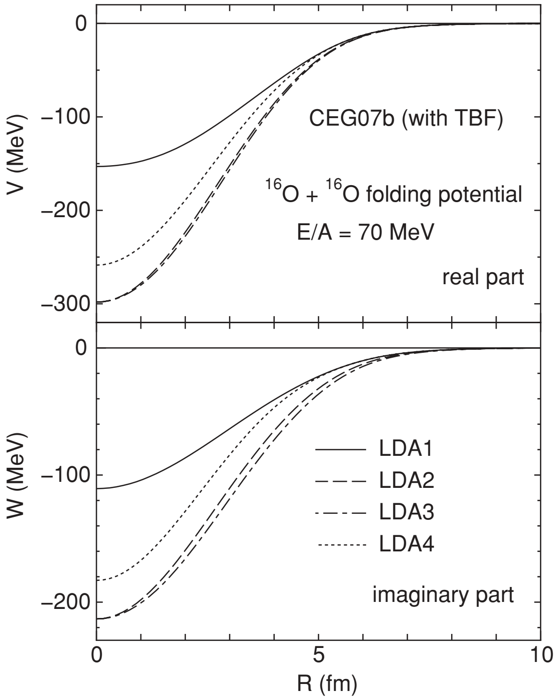

FIG. 4. Same as Fig. 1, but for the comparison with various LDA prescriptions for CEG07b.

Figure 4 shows the real and imaginary parts of the calculated FMP with CEG07b for the $^{16}\mathrm{O}+{}^{16}\mathrm{O}$ elastic scattering at $E/A = 70$ MeV in the cases of adopting the four types of the local density. The effect of different definitions of the local density is clearly seen in both the real and imaginary parts of the FMP over the whole range of internuclear distance. The FMPs obtained by LDA2 and LDA3 are found to be very deep compared with those by LDA1 and LDA4. In the former cases, the local densities are defined by average-type definitions: either the geometric average (LDA2) or the arithmetic one (LDA3) of the densities of colliding nuclei, called here the average-density approximation (ADA). In the ADA, the interacting nucleon pair feels lower local densities than in the FDA, which implies that the strength of the G matrix evaluated at such lower densities becomes stronger than that evaluated at higher densities in the case of the FDA. In other words, the Pauli principle as well as the TBF (particularly the TBR) effect, which are expected to act to reduce the G-matrix strength at the high-density region, do not play significant roles in the ADA prescriptions; hence, the ADA leads to deeper FMPs. On the other hand, the FMP calculated with LDA4 definition gives a deeper potential than the FMP obtained by the use of LDA1 (namely, the FDA) in the medium- and short-range regions where $\rho_1 + \rho_2$ exceeds ρ_0, while around the nuclear surface region, the FMPs of LDA1 and LDA4 have almost the same strength and shape because both LDA1 and LDA4 use the same local density, $\rho_1 + \rho_2$, in such a lower density region. One may notice that the FMP obtained with LDA4 is weaker than those with the ADAs (LDA2 and LDA3).

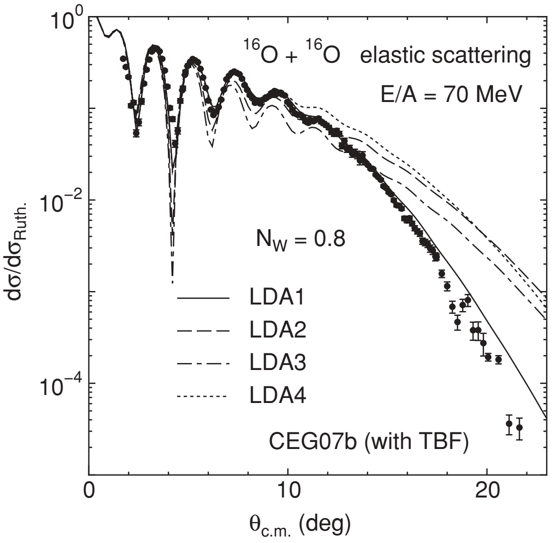

FIG. 5. Same as Fig. 2, but for the comparison with various LDA prescriptions for CEG07b.

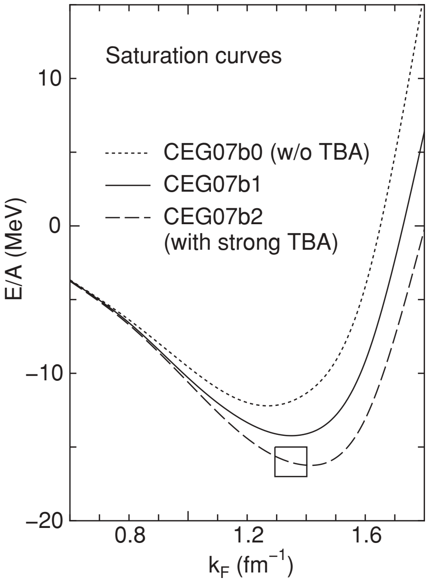

FIG. 6. Effects of the three-body attractive force in the saturation curves obtained by the G-matrix calculation.

This is partly because the nuclear density in the ^{16}O nucleus does not reach the saturation value, ρ_0, even at the nuclear center. Another probably more general reason for this is closely connected to the finite-range nature of the G-matrix interaction used.

Figure 5 compares the cross sections calculated with the four kinds of FMPs obtained by different definitions of the local density. The deep FMPs given by the ADA (LDA2 and LDA3) do not reproduce the data at all. The FMP with LDA4 also fails to reproduce the data at backward angles, although the fit to the data at forward angles is not so bad because the tail part of the FMP with LDA4 has a reasonable strength and shape similar to those of the FMP with the FDA. We also confirmed that no reasonable fit to the data was obtained by the FMPs with LDA2–4 no matter how the imaginary part of the FMP was renormalized. A comparison between the FDA and the ADA was also made in Ref. [19] in the FMP calculation for the α-nucleus elastic scattering with the use of the CDM3Y6 interaction [12] having a phenomenologically parametrized density dependence, where the FDA turned out to be a better approximation of the overlap density.

The validity of the FDA is understood qualitatively by considering that the colliding nuclei can overlap into each other without the disturbance due to the Pauli principle in such a high energy as $E/A = 70$ MeV. Then, the G-matrix interaction in the high-density region over the normal density, including the strong TBR, contributes to the folding potential. The importance of the TBF discussed in the previous subsection is revealed with the use of the FDA prescription, which properly evaluates the local density at the high-density region. This confirms the validity of the folding model method used to probe the nuclear-matter properties at the high-density region and, hopefully, to extract the nuclear-matter incompressibility K [11,12,34] from the refractive nucleus-nucleus scattering.

3. Strength of three-body attractive force

In this section, we analyze the effect of the TBA force. CEG07b includes the effect of the TBA in the form of the Fujita-Miyazawa diagram. Indeed, the TBA is known to originate from various diagrams, such as the Δ and Roper excitations. In this paper, we assume that the TBA is due only to the Fujita-Miyazawa diagram with the Δ resonance, because the Δ resonance is known to have the most important contribution to the TBA. On this assumption, we investigate the effect of the TBA strength on the nuclear matter properties as well as on the scattering cross section, by changing the TBA cutoff parameter. In this section, we name the three types of CEG07b with various TBA parameters as CEG07b0, CEG07b1, and CEG07b2. CEG07b1 is the original CEG07b itself. CEG07b0 includes no three-body attractive force. CEG07b2 has a stronger TBA than CEG07b1; this TBA is adapted so that the most reasonable saturation curve is reproduced, as shown in Fig. 6.

Figure 7 compares the calculated cross sections with the FMPs obtained by the three types of CEG07b. The effect of the TBA force is clearly seen in the saturation curves as shown in Fig. 6. However, this effect can be compensated for by changing the renormalization factor N_W for the imaginary part by about 5%, as shown in Fig. 7. The role of the TBA effect is not clearly seen for nucleus-nucleus elastic scattering, although the Δ resonance (the Fujita-Miyazawa diagram) is known to be the most important TBA effect and clearly seen in the saturation curves in Fig. 6.

4. Effect of ω-rearrangement diagram

In this section, we investigate the effect of the ω-rearrangement diagram for the $^{16}\mathrm{O} + {}^{16}\mathrm{O}$ elastic scattering. To investigate the effect of the ω-rearrangement term, two types of CEG07c with and without the ω-rearrangement term effect are called CEG07c1 and CEG07c2, respectively. CEG07c1 is

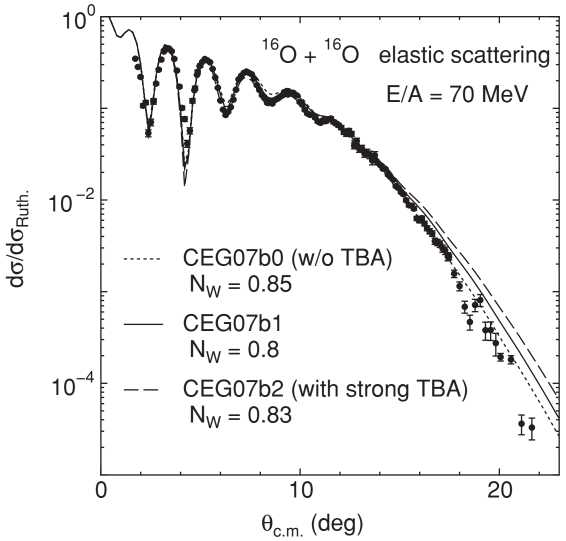

FIG. 7. Same as Fig. 2, but for comparison with the effect of the three-body attractive force.

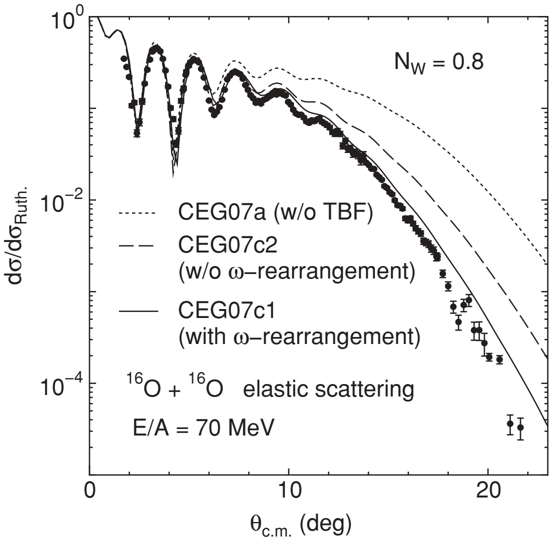

FIG. 9. Same as Fig. 2, but for the comparison with the effect of the ω rearrangement.

the original CEG07c itself. Then, we test the three types of G-matrix interaction: CEG07a, CEG07c1 and CEG07c2. In the DFM calculations, we parametrize the calculated values of $\bar{\mathcal{K}}$ in Ref. [7] as a function of ρ:

$$\bar{\mathcal{K}} = 0.0898 + 0.179\rho. \tag{19}$$

Figure 8 shows the comparison of the FMPs calculated with CEG07a, CEG07c1, and CEG07c2 for the $^{16}\mathrm{O} + {}^{16}\mathrm{O}$ system at $E/A = 70$ MeV. The TBF effect is also clearly seen in the real part of the FMP over the whole range of internuclear distance by the comparison of CEG07a with CEG07c2, as in the case of Fig. 1, although the repulsive contribution of the TBF is slightly smaller than that seen in Fig. 1 when CEG07b was used. On the other hand, the TBR effect on the imaginary part of the FMP (the difference between the dotted and dashed curves) is very small. The effect of the ω rearrangement is seen in both real and imaginary parts of FMP and reduces the strength of the FMP by about 10% at $R = 0$.

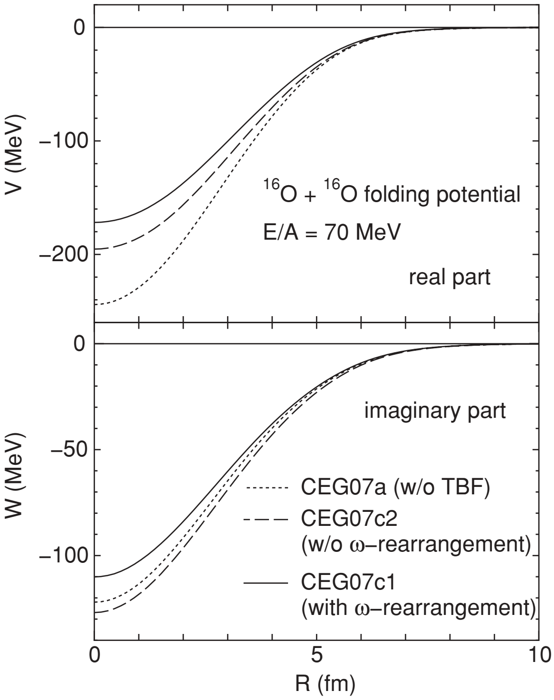

FIG. 8. Same as Fig. 1, but for the comparison with the effect of the ω rearrangement.

Figure 9 compares the cross sections calculated with the FMPs obtained by CEG07a, CEG07c1, and CEG07c2. Here, the renormalization factor N_W is taken to be the same value 0.8 as that in the calculations with CEG07b shown in Fig. 2. The effect of the TBF is clearly seen in the large change of cross sections from the dotted curve to the dashed one. However, the dashed curve with CEG07c2 cannot give a satisfactory fit to the experimental data at the middle to backward angles because of a slightly weaker TBR effect included in this interaction. A further inclusion of the effect of the ω-rearrangement diagram almost compensates for the discrepancy between the dashed curve and the experimental data, as shown by the solid curve in Fig. 9. This implies that some part of the TBR contribution can be substituted by another repulsive contribution such as the ω-rearrangement term. Because our modeling for the TBR effect is of a phenomenological character, it is difficult to divide strictly the repulsive effect into the real three-body repulsion and the other correlation. CEG07c should be considered as one possible model for the needed repulsive effect. There is little to choose from between CEG07b and CEG07c in our present analyses.

5. *Comparison with CDM3Y6*

The CDM3Y6 interaction [12] is one of the reliable and successful effective density-dependent NN interactions used in the DFM. CDM3Y6 has only the real part, and hence it has to be accompanied by a phenomenological imaginary potential. However, it would be meaningful to compare it with the real part of the FMP obtained by the present complex CEG07 interaction. In this comparison, we assume two models: one uses the same imaginary potential as that obtained by the FMP with CEG07b, which we call model A,

$$U_{\mathrm{opt}}(R) = V_{\mathrm{CDM3Y6}}(R) + i N_W W_{\mathrm{CEG07b}}(R), \tag{20}$$

and another uses the imaginary potential having the same shape as that of the real part of the FMP obtained with CDM3Y6, which we call model B,

$$U_{\mathrm{opt}}(R) = (1 + i N_W) V_{\mathrm{CDM3Y6}}(R). \tag{21}$$

Here, the N_W value is taken to reproduce the experimental data of elastic cross sections in each case.

The CDM3Y6 interaction has three-range Yukawa form factors. In this paper, we have calculated the DFM potential based on the LDA prescription as follows:

$$\rho = \rho_1\left(\boldsymbol{r}_1 + \tfrac{1}{2}\boldsymbol{s}\right) + \rho_2\left(\boldsymbol{r}_2 - \tfrac{1}{2}\boldsymbol{s}\right). \tag{22}$$

However, it is technically difficult to evaluate the local density at “midpoint” of the interacting nucleon pair in the projectile and target, as long as we use the interaction having a Yukawa form factor. For this reason, in this section, the double-folding calculation is performed in the same manner as in Ref. [22] by defining the local density as

$$\rho = \rho_1(\boldsymbol{r}_1) + \rho_2(\boldsymbol{r}_2), \tag{23}$$

only when we calculate the direct part. In other words, the evaluating point of the local density for the direct part is calculated at “each point” of the interacting nucleon pair in this section.

First, we test the difference of the evaluating point of the local density as defined in Eqs. (22) and (23). Figure 10 shows the difference of the calculated elastic cross sections with respect to the evaluating point of the local density in the case of CEG07b. The N_W values for each calculation have been taken to be the value given in the figure so as to reproduce the elastic cross section. Both calculations reproduce well the measured cross section data with the use of about 10% different renormalization factors for the imaginary part. Thus, we conclude that one needs not seriously care about the spatial position of evaluating the local density in this system, as long as we renormalize the imaginary potential strength.

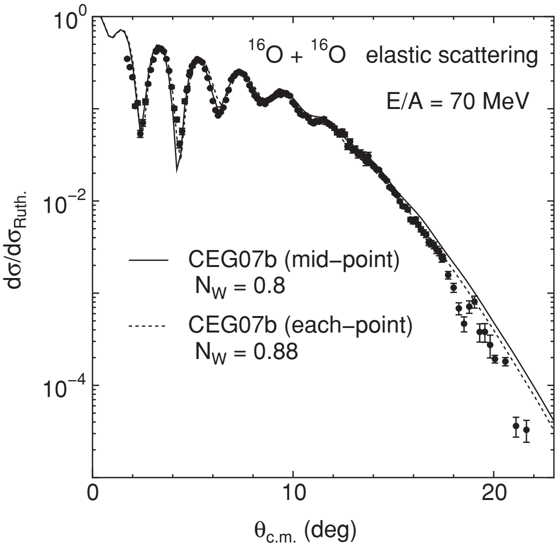

FIG. 10. Same as Fig. 2, but for the difference with respect to the evaluating point of the local density in the case of CEG07b.

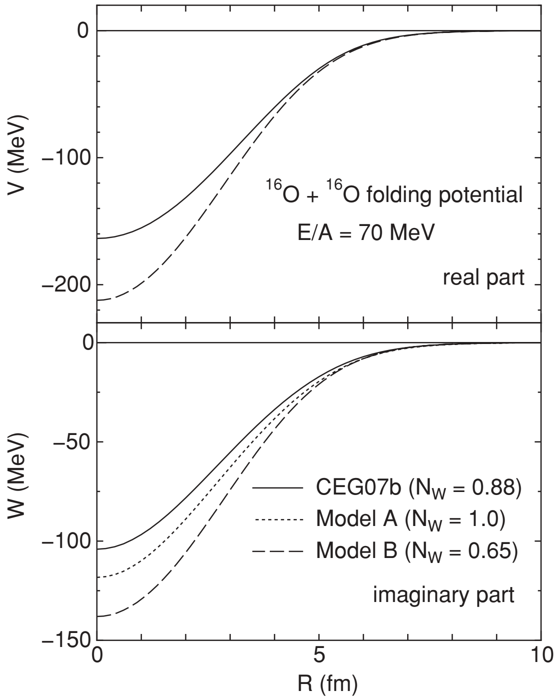

FIG. 11. Same as Fig. 1, but for the comparison of CEG07b with CDM3Y6.

Next, we compare the FMP calculated with CEG07b and CDM3Y6, where, in both cases, the local density is evaluated by the each-point prescription [Eq. (23)] when we calculate the direct part. The difference of the FMPs derived from CEG07b and CDM3Y6 is seen at the short- and middle-range parts, as shown in Fig. 11. The real part of the FMP with CDM3Y6 is deeper than that with CEG07b by about 50 MeV at $R = 0$. However, the difference appears only at the most backward angles in the elastic cross sections, as shown in Fig. 12. The FMP calculated with CDM3Y6 gives almost the same results in the cross section (the dotted and dashed curves), irrespective of the imaginary potential model used. Here, we note that the complex G-matrix interaction CEG07 derived from the theoretical framework gives the result similar to or better than the phenomenological density-dependent effective interaction CDM3Y6.

B. Analysis of ^{16}O elastic scattering by other target nuclei

In this section, we analyze the elastic scattering of ^{16}O by the ^{12}C, ^{28}Si, and ^{40}Ca target nuclei at $E/A = 93.9$ MeV with the use of CEG07a, CEG07b, and CEG07c interactions.

Figure 13 shows the ^{16}O elastic-scattering cross sections for the ^{12}C, ^{28}Si, and ^{40}Ca targets at $E/A = 93.9$ MeV. The difference between CEG07b and CEG07c is small in all systems, and both reproduce well the elastic cross sections

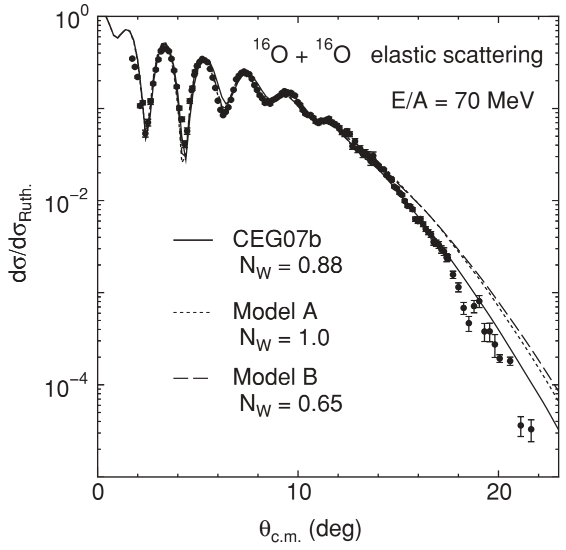

FIG. 12. Same as Fig. 2, but for the comparison of CEG07b with CDM3Y6.

up to the backward angles. The effect of the TBF is clearly seen in the cross sections, as in the case of the ^{16}O + ^{16}O scattering shown in Figs. 2 and 9. No reasonable fit to the data is obtained by the FMP calculation with CEG07a (without TBF effect), no matter how we change the value of N_W, which is also the same as in the case of the ^{16}O target shown in Fig. 3. For the ^{28}Si target, the fit to the experimental data is not necessarily perfect at large angles. This may be related to the fact that the ^{28}Si nucleus presents a slightly stronger absorption ($N_W = 0.9$) to the incident ^{16}O nucleus compared with other target nuclei ($N_W \approx 0.75$). Since the ^{28}Si nucleus is known to be a very deformed nucleus that shows a typical rotational band in the excitation spectrum, it may be reasonable to expect that additional absorption should be induced dynamically by collective excitation of the ^{28}Si nucleus in the collision with ^{16}O. This kind of dynamical effect may not be represented by the imaginary part of the G-matrix interaction evaluated in the nuclear matter. This would be one of the reasons for a slightly larger value of the optimum N_W for the ^{28}Si target ($N_W = 0.9$) than that for other targets ($N_W \approx 0.75$). In fact, we have confirmed that a better fit up to the backward angles is obtained by a coupled-channel (CC) calculation based on the present FMP potential in the case of the ^{28}Si target with a smaller value of N_W. The CC analyses will be reported in forthcoming publications.

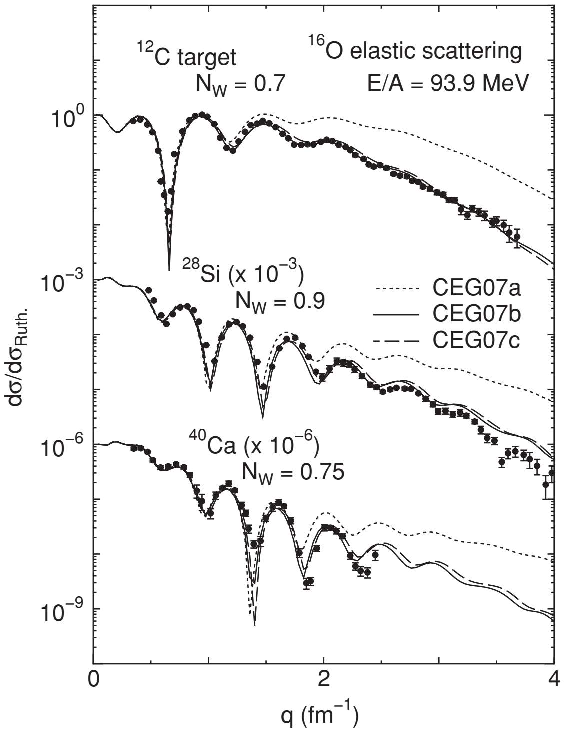

FIG. 13. Rutherford ratio of the cross sections for elastic scattering of ^{16}O by the ^{12}C, ^{28}Si, and ^{40}Ca targets at $E/A = 93.9$ MeV, calculated with the three types of complex G-matrix interactions, which are compared with the experimental data from Ref. [35]. The abscissa is the momentum transfer q defined as $q = 2k \sin \frac{\theta}{2}$, where k is the asymptotic momentum.

C. ^{12}C + ^{12}C system

In this section, we analyze elastic scattering of the ^{12}C + ^{12}C system studied at $E/A = 135$ MeV. The ^{12}C + ^{12}C system is an interesting system and the most frequently studied light heavy-ion system.

Figures 14 and 15 show the FMPs and elastic-scattering cross sections for the ^{12}C + ^{12}C system at $E/A = 135$ MeV, respectively. The effect of the TBF is also clearly seen for

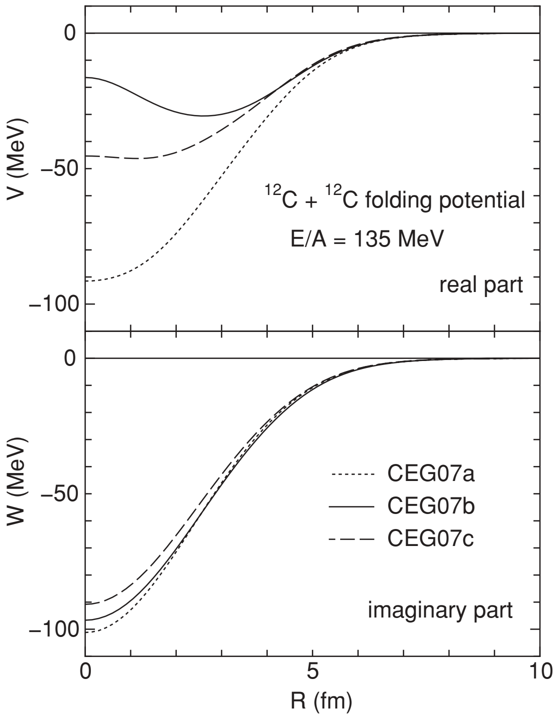

FIG. 14. Real and imaginary parts of the FMP for the ^{12}C + ^{12}C elastic scattering at $E/A = 135$ MeV, obtained with the three types of complex G-matrix interactions.

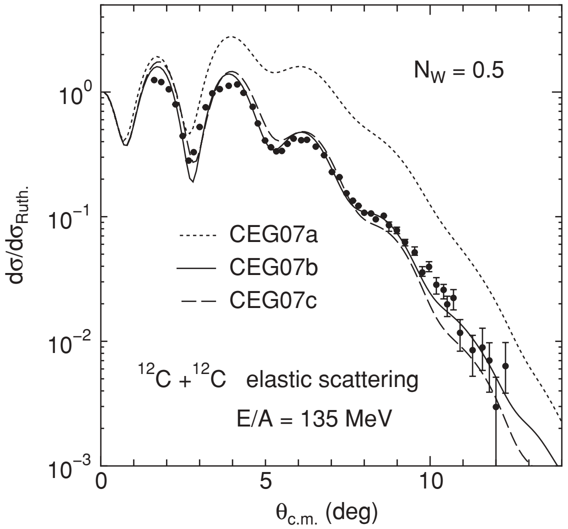

FIG. 15. Rutherford ratio for the $^{12}\mathrm{C} + {}^{12}\mathrm{C}$ system at $E/A =$ 135 MeV calculated with the three types of complex G-matrix interactions, which are compared with the experimental data from Ref. [36].

the $^{12}\mathrm{C} + {}^{12}\mathrm{C}$ elastic scattering as in the other systems. The difference between CEG07b and CEG07c is enhanced at the inner part of the real potential compared with the $^{16}\mathrm{O} + {}^{16}\mathrm{O}$ case at $E/A = 70$ MeV, and the fit to the experimental data for the cross sections looks apparently better for CEG07b than CEG07c (Fig. 15). This could be related to the weaker absorption (the optimum value of $N_W = 0.5$) for this system than for the other systems discussed so far, although the origin of the weaker absorption for this system is not clear at this stage. It is worth mentioning that a similar trend of weaker absorption for elastic scattering relevant to the ^{12}C nucleus was also pointed out in a previous study [37].

D. Energy dependence

The energy dependence of the G-matrix interaction is automatically given in the G-matrix calculation. In fact, the energy dependence of CEG07 is found to be very reliable at least in the energy range of $E/A = 70 \sim 135$ MeV as shown in preceding sections. Of course, the energy dependence of the FMP is also generated by the space-exchange terms in the folding procedure. It is difficult to judge which of the two origins plays an important role.

In this section, we test the energy dependence of the interactions for the $^{16}\mathrm{O} + {}^{16}\mathrm{O}$ elastic scattering at various energies. In the previous section, we saw that the difference between CEG07b and CEG07c becomes enhanced (particularly in the real FMP) at higher energies ($E/A = 135$ MeV) for the $^{12}\mathrm{C} + {}^{12}\mathrm{C}$ case. Therefore, we expect that the difference may become more important at higher energies. Figure 16 shows the $^{16}\mathrm{O} + {}^{16}\mathrm{O}$ elastic-scattering cross sections at $E/A =$ 100, 200, 300, and 400 MeV. Here, we have fixed the N_W value to unity for simplicity because of the lack of experimental data. At $E/A = 100$ MeV, the role of the TBF is clearly seen, while the difference between CEG07b and CEG07c cannot be seen, same as what we saw in the previous sections. However, at $E/A = 200$ MeV, the difference of three types of CEG07 becomes small. When we go to higher energies, $E/A = 300$ and 400 MeV, an interesting result appears. It is easy to distinguish among the cross sections obtained with the three types of CEG07 at these energies. Especially, the difference between CEG07b and CEG07c is clearly seen in the cross sections at $E/A = 400$ MeV, although this difference could not be distinguished at $E/A = 70 \sim 135$ MeV shown in the previous sections. The large difference is caused by the large difference of the FMPs obtained with the three types of CEG07 interaction, as shown in Fig. 17. The real parts of FMP with CEG07b and CEG07c have a difference of about 100 MeV at $R = 0$, and this large difference can no longer be compensated for by only changing the renormalization factor N_W for the imaginary potential. Here, we note that the real part of all FMPs becomes repulsive ($V > 0$). The detailed survey for this repulsive nature will be reported in forthcoming publications.

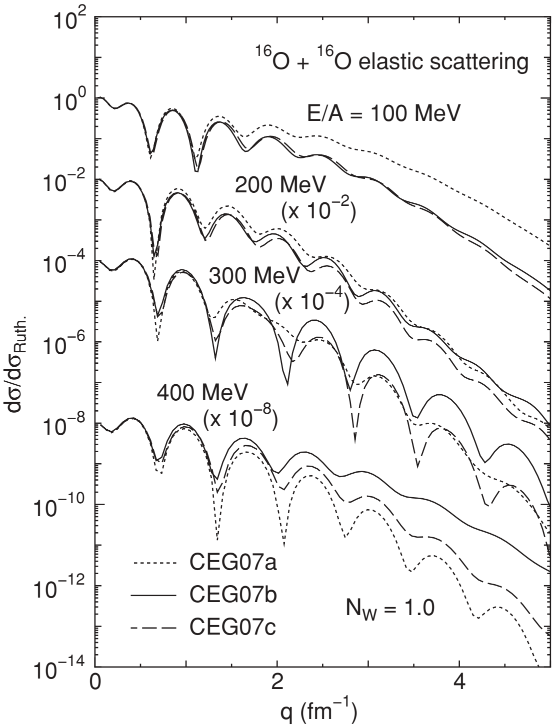

FIG. 16. Rutherford ratio of the cross sections for the $^{16}\mathrm{O} + {}^{16}\mathrm{O}$ elastic scattering at $E/A = 100$, 200, 300, and 400 MeV calculated with the three types of complex G-matrix interactions. The N_W value is fixed to 1.0 for all the calculations.

It should be noted that the real origin of the TBR is not yet established. In our modeling, the TBR effect is represented as a density-dependent two-body force, which is of no energy dependence. As is well known, G matrices become similar to the free-space T matrices with the increase of energy, which is ensured qualitatively in the G-matrix formalism. Then, a possible conjecture is that the TBR contributions disappear in such an energy region, because a scattering pair has almost no overlap with the third nucleon inside the nuclear medium. If so, it might be likely that CEG07a reproduces the experimental data rather than CEG07b/c in the case of high-energy scattering. It can be said that experimental studies

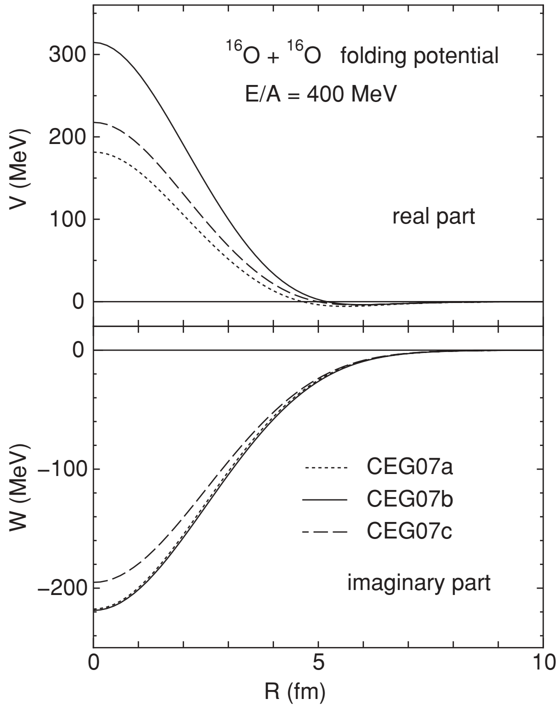

FIG. 17. Real and imaginary parts of the FMP for the $^{16}\text{O}+{}^{16}\text{O}$ elastic scattering at $E/A = 400$ MeV, obtained with the three types of complex G-matrix interactions.

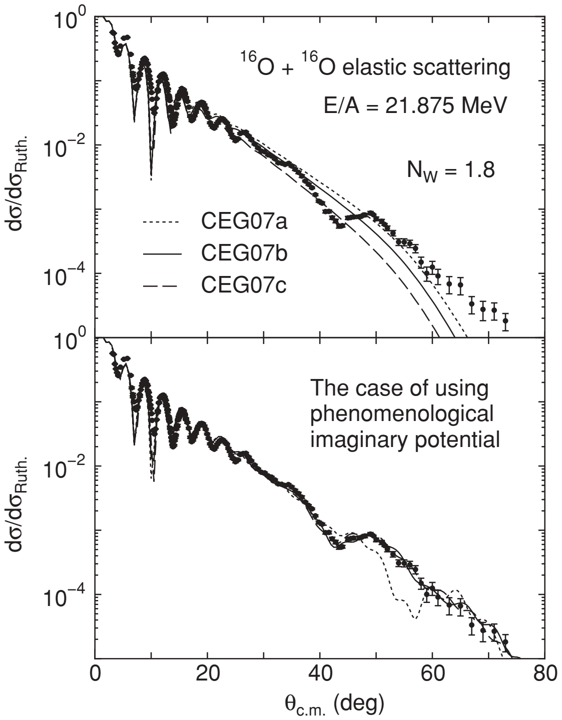

FIG. 18. Rutherford ratio of cross sections for the $^{16}\text{O}+{}^{16}\text{O}$ elastic scattering at $E/A \approx 22$ MeV ($E_{\text{lab}} = 350$ MeV). Upper: cross sections calculated with the complex FMP with CEG07a, CEG07b, and CEG07c. The N_W value is fixed to 1.8. Lower: cross sections calculated with the real part of the FMP and the phenomenological imaginary potential. The experimental data are from Refs. [38,39].

of such an energy dependence will provide a way to resolve the origin of the TBR-like effect.

On the other hand, we have also applied the FMP with CEG07 to the $^{16}\text{O}+{}^{16}\text{O}$ elastic scattering at the energy region lower than $E/A = 70$ MeV. In this paper, we show the typical case of $E/A \approx 22$ MeV($E_{\text{lab}} = 350$ MeV), where the nuclear rainbow phenomenon is clearly seen. At this energy, we have adopted the each-point prescription [Eq. (23)] for evaluating the local density in the direct part, because it is found to be a better approximation at energies lower than the midpoint one [Eq. (22)], although their difference is small at higher energies, as we saw in Fig. 10. The upper panel of Fig. 18 shows the results. Although the forward-angle data are well reproduced in the same quality as for the higher energy cases, the calculated cross sections do not reproduce the experimental data at this energy around the middle and backward angles. In this case, we need to strengthen the imaginary parts of the FMPs by setting the value of N_W to be 1.8 to obtain an overall optimum fit to the data. We have also tested the FMP with CEG07 to the $^{16}\text{O}+{}^{16}\text{O}$ elastic scattering at $E/A \approx 15$, 30, and 44 MeV ($E_{\text{lab}} = 250$, 480, and 704 MeV), but all the calculated cross sections do not reproduce the data at backward angles.

Figure 19 shows the real and imaginary parts of the FMPs with CEG07 at $E/A \approx 22$ MeV($E_{\text{lab}} = 350$ MeV). The real parts of the FMPs with CEG07b and CEG07c are very similar to the Kondō-A potential [29], which is one of the best phenomenological optical potentials determined to reproduce the rainbow scattering at this energy. They are also close to the renormalized FMP with DDM3Y, which also reproduces the rainbow scattering, given in Fig. 3 of Ref. [21]. This suggests that the failure of the present FMP calculation at the backward angles may be due to a defect of the imaginary part. To confirm this, we have replaced the imaginary part of the FMP by the following phenomenological one $W_{\text{phenom.}}$ as

$$U_{\text{opt}}(R) = V_{\text{CEG07}}(R) + i\,W_{\text{phenom.}}(R), \tag{24}$$

where

$$W_{\text{phenom.}}(R) = -W_0 f(x_0) + 4W_{\text{d}}\frac{df(x_{\text{d}})}{dx_{\text{d}}},$$

$$f(x) = \frac{1}{1+\exp(x)},$$

$$x_{0,\text{d}} = (R - R_{0,\text{d}})/a_{0,\text{d}},$$

and the imaginary-potential parameters are optimized so as to reproduce the experimental data. Here, we have used an automatic potential search code ALPS [40] to search for the best-fit values of the parameters, and they are shown in Table II.

TABLE II. Parameters for the phenomenological imaginary potential, used in the lower panel of Fig. 18.

	W_0	R_0	a_0	W_d	R_d	a_d
CEG07a	30.93	5.667	0.6958	14.54	4.539	0.2102
CEG07b	25.13	5.844	0.6505	12.02	4.736	0.2561
CEG07c	26.54	5.684	0.6698	9.335	4.650	0.2476

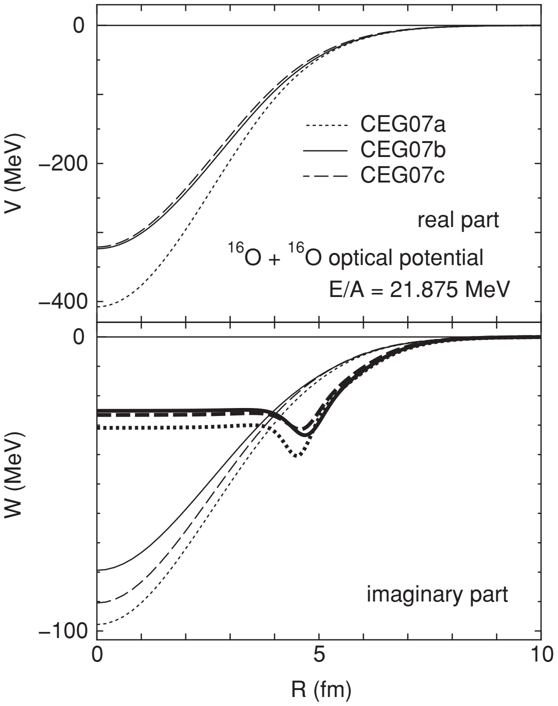

FIG. 19. Real and imaginary parts of the FMP for the $^{16}\mathrm{O}+{}^{16}\mathrm{O}$ elastic scattering at $E/A \approx 22$ MeV($E_{\mathrm{lab}} = 350$ MeV). For the imaginary part, the three kinds of thin curves are the FMPs with the three types of the complex G-matrix interactions and the bold curves are the phenomenological imaginary potentials, associated with the corresponding real FMP shown in the upper panel.

Here, we note that unlike most of the previous folding-model analyses [11,12,19,21,25,34], no renormalization is made on the real part. In this constraint, the calculated cross sections by the FMPs with CEG07b and CEG07c reproduce well the experimental data up to the most backward angles including the Airy diffraction followed by the nuclear-rainbow bump and the rapid falloff toward the backward angles, as shown in the lower panel of Fig. 18. On the other hand, the calculation with CEG07a does not reproduce the typical nuclear-rainbow structure in this angular region. This implies that the effect of the TBF is also clearly seen in this system, although the phenomenological imaginary potential is used, and that the present folding model still gives a proper account of the real part of the FMP in this low-energy region.

Here, let us pay attention to the imaginary parts of the potential used in Fig. 18. In the lower panel of Fig. 19, we compared the imaginary part of the FMPs obtained by CEG07 with the phenomenological imaginary potentials used in the lower panel of Fig. 18. The thin curves are the FMPs calculated with CEG07 (not being renormalized) and the bold curves are the phenomenological imaginary potentials. It is understood that the large difference of the calculated cross sections at large angles shown in the upper and lower panels of Fig. 18 is mainly caused by the difference of the imaginary part. The imaginary part of the FMP around the tail part is smaller than the phenomenological one; thus, we needed to strengthen the imaginary part of the FMP with $N_W = 1.8$ to reproduce the experimental data. On the other hand, the strength of the imaginary part of the FMP at the inner part is larger than the phenomenological one. This would be closely related to the fact that in the G-matrix calculation of deriving CEG07, the Pauli-exclusive principle was evaluated by the standard single-Fermi sphere prescription. This prescription is valid for the calculation of the FMP for NA systems. However, for AA systems, this prescription may not necessarily be suited for a proper account of the Pauli-forbidden region, particularly for the high-density region of low-energy collisions; and, in such situations, it would be more realistic to use the double-Fermi spheres to account for the Pauli-forbidden region as was done in Refs. [41–43], in particular at the lower energy region, which is one of the important future works.

IV. SUMMARY

In summary, we first analyzed the elastic scattering of the $^{16}\mathrm{O}+{}^{16}\mathrm{O}$ system at $E/A = 70$ MeV with the use of CEG07a, CEG07b, and CEG07c interactions, where the latter two include the effect of the TBF (TBA + TBR). The effect of the TBF is seen clearly in the real potential, where the potential is pushed upward remarkably by the TBR contribution in the high-density region owing to the prescription of the frozen-density approximation (FDA). Then, the DFM with CEG07b and CEG07c including the TBR effect nicely reproduces the observed $^{16}\mathrm{O}+{}^{16}\mathrm{O}$ elastic-scattering cross sections over the whole angular region. On the other hand, the DFM with CEG07a derived only from the two-body interaction gives no reasonable fit to the data no matter how the value of N_W is changed.

In addition, we have tested the validity of the FDA for the local density approximation (LDA) prescription to confirm the conclusion that the effect of the TBF has an important role for AA systems. The four types of LDA prescriptions are tested: the FDA, the averaged density approximation (ADA) (geometric average or arithmetic one), and the cutting density approximation (CDA). The ADA gives a too deep potential compared with the FDA, which leads to no reasonable fit to the experimental data. The CDA also leads to a too deep potential compared with the FDA at the inner region, and the calculated potential does not reproduce the data at backward angles. The validity of the FDA confirms that the folding model method using the complex G-matrix interaction with the TBF evaluated up to the high-density region ($\rho \approx \rho_0$) is quite useful in probing the high-density nuclear-matter properties and, hopefully, to extract the nuclear-matter incompressibility K [11,12,34] from the analyses of nucleus-nucleus scattering.

The effect of the Δ-resonance TBA that is described by the Fujita-Miyazawa diagram has been tested. The TBA effect is clearly seen in the saturation curves and has an important role in satisfying the saturation point. However, the effect can be compensated for by changing the renormalization factor N_W for the imaginary part by about 5% for the $^{16}\mathrm{O}+{}^{16}\mathrm{O}$ elastic scattering at $E/A = 70$ MeV. It is understood that the TBR-like effect of the TBF has a decisive role in nucleus-nucleus elastic scattering.

The effect of the ω-rearrangement term has also been tested for the same system. CEG07c was designed to include a weaker TBR effect than the CEG07b, so the experimental data are reproduced well with the additional inclusion of the repulsive effect originating from the ω-rearrangement term. When the ω-rearrangement term effect is switched off from CEG07c, the effect appears in the cross sections at the backward angles. It should be considered that CEG07c is one of the possible models for the TBR-like repulsive effect.

Then, the FMPs calculated with CEG07b are compared with one of the CDM3Y interactions. The complex G-matrix interaction CEG07 derived from the theoretical framework gives a result that is similar to or better than that of the phenomenological density-dependent effective interaction CDM3Y6, although CEG07b and CDM3Y6 show a substantial difference in the calculated real potential.

We also apply the folding model potential calculated with CEG07a–CEG07c in the framework of the FDA for other systems: the $^{16}\mathrm{O}+^{12}\mathrm{C}$, $^{16}\mathrm{O}+^{28}\mathrm{Si}$, and $^{16}\mathrm{O}+^{40}\mathrm{Ca}$ systems at $E/A = 93.9$ MeV and the $^{12}\mathrm{C}+^{12}\mathrm{C}$ system at $E/A = 135$ MeV. All the cross sections can be reproduced by the calculated FMPs with CEG07b and CEG07c (with the TBF). The FMP calculated with CEG07a (without the TBF) cannot reproduce the data as in the case of the $^{16}\mathrm{O}+^{16}\mathrm{O}$ system. CEG07a gives a too deep FMP to reproduce the data. The effect of the TBF is also clearly seen at FMPs and elastic cross sections for these systems as in the case of the $^{16}\mathrm{O}+^{16}\mathrm{O}$ at $E/A = 70$ MeV. Then, we demonstrated the energy dependence of CEG07 for the $^{16}\mathrm{O}+^{16}\mathrm{O}$ system at various energies. The difference between CEG07b and CEG07c is clearly seen in the cross sections at $E/A = 300$ and 400 MeV, although this difference is not clearly seen at the lower energies.

In conclusion, we have made an important step toward establishing a microscopic model to construct reliable complex OMP by the DFM with CEG07 for AA systems.

ACKNOWLEDGMENTS

The authors acknowledge Professor Dao T. Khoa for providing with the numeral data of the $^{16}\mathrm{O}+^{16}\mathrm{O}$ elastic scattering. The authors would like to thank Professor Y. Iseri for allowing them to use the ALPS computer code for the optimum potential research done in this work. One of the authors (T.F.) is supported by the Japan Society for the Promotion of Science for Young Scientists.

APPENDIX

In this appendix, we give the parameters of the CEG07b interaction fitted as a function of ρ to be used in the DFM calculation. The CEG07 interactions are parametrized by the three-range Gaussian form defined by

$$v^{ST}(s, \rho, E/A) = \sum_{k=1}^{3}\sum_{i=1}^{4} v_{ik}^{ST}(E/A)\rho^{i-1}\exp\left(-\frac{s^2}{\lambda_k^2}\right), \tag{A1}$$

v^{ST} is the strength for each spin-isospin component ($S = 0$ or 1 and $T = 0$ or 1) of the G-matrix interaction. Here, λ_1, λ_2, and λ_3 are fixed to be 0.5, 0.9, and 2.5, respectively. The parameters $v_{ik}^{ST}(E/A)$ for CEG07b at $E/A = 70$, 80, 100, 120, and 140 MeV are given in Tables III–VII. Here, we note that these parameters are fitted to the numerical data of calculated G-matrix interactions up to $k_F = 1.8\ \mathrm{fm}^{-1}(\rho \approx 0.39\ \mathrm{fm}^{-3})$. In this paper, the direct (v_D) and exchange (v_{EX}) parts of the G-matrix interaction are written as

$$v_{D,\mathrm{EX}} = \tfrac{1}{16}(\pm v^{00} + 3v^{01} + 3v^{10} \pm v^{11}), \tag{A2}$$

where the upper and lower parts of the double-sign symbols correspond to the direct (D) and exchange (EX) parts, respectively.

TABLE III. Parameters $v_{ik}^{ST}(E/A)$ of Eq. (A1) for real and imaginary components of CEG07b at $E/A = 70$ MeV.

		Real part						Imaginary part			
k	i	$S = 0, T = 0$	$S = 0, T = 1$	$S = 1, T = 0$	$S = 1, T = 1$	k	i	$S = 0, T = 0$	$S = 0, T = 1$	$S = 1, T = 0$	$S = 1, T = 1$
1	1	-9.9676×10^{1}	4.8220×10^{2}	4.2388×10^{2}	-1.4588×10^{3}	1	1	5.2529×10^{1}	3.4087×10^{2}	6.4816×10^{2}	-1.8251×10^{2}
	2	7.2393×10^{3}	1.6845×10^{3}	7.5453×10^{3}	8.6225×10^{3}		2	-1.2811×10^{3}	-2.6123×10^{3}	-1.6809×10^{3}	7.7712×10^{2}
	3	-2.3837×10^{4}	-6.8168×10^{3}	-2.7942×10^{4}	-2.8303×10^{4}		3	5.3901×10^{3}	8.0465×10^{3}	-1.6936×10^{3}	-1.6198×10^{3}
	4	3.3435×10^{4}	8.3105×10^{3}	3.1555×10^{4}	3.3185×10^{4}		4	-6.6116×10^{3}	-9.0074×10^{3}	5.4425×10^{3}	1.7246×10^{3}
2	1	1.2835×10^{2}	-1.8113×10^{2}	-1.2214×10^{2}	-5.6815×10^{0}	2	1	-1.5410×10^{1}	-1.3296×10^{2}	-3.1979×10^{2}	-1.1765×10^{1}
	2	3.2444×10^{2}	-2.8817×10^{2}	-3.0093×10^{3}	3.1284×10^{2}		2	-7.6499×10^{1}	1.1503×10^{3}	1.2114×10^{3}	-9.1195×10^{0}
	3	-5.0655×10^{2}	2.1482×10^{3}	1.2032×10^{4}	-5.1778×10^{2}		3	4.0189×10^{2}	-3.8231×10^{3}	-9.1269×10^{2}	8.4879×10^{1}
	4	4.6701×10^{2}	-2.9074×10^{3}	-1.4214×10^{4}	5.8398×10^{2}		4	-3.8454×10^{2}	4.4178×10^{3}	-5.9724×10^{2}	-3.2118×10^{1}
3	1	7.8360×10^{0}	-3.2201×10^{0}	-3.6574×10^{0}	4.8937×10^{-1}	3	1	-1.1343×10^{0}	-1.0788×10^{0}	-1.6022×10^{0}	-5.2176×10^{-1}
	2	-2.8749×10^{0}	4.7782×10^{-1}	2.5360×10^{0}	1.0576×10^{-2}		2	4.0221×10^{0}	9.2598×10^{0}	1.6057×10^{1}	2.8866×10^{0}
	3	1.2581×10^{1}	-2.1102×10^{0}	1.4408×10^{0}	-4.0424×10^{-1}		3	-1.7094×10^{1}	-3.2307×10^{1}	-6.7185×10^{1}	-1.0490×10^{1}
	4	-1.5349×10^{1}	3.9915×10^{0}	-9.4313×10^{0}	7.6793×10^{-1}		4	3.0601×10^{1}	3.8871×10^{1}	8.3651×10^{1}	1.5009×10^{1}

TABLE IV. Same as Table III, but at $E/A = 80$ MeV.

		Real part						Imaginary part			
k	i	$S = 0, T = 0$	$S = 0, T = 1$	$S = 1, T = 0$	$S = 1, T = 1$	k	i	$S = 0, T = 0$	$S = 0, T = 1$	$S = 1, T = 0$	$S = 1, T = 1$
1	1	-5.0786×10^{1}	4.6473×10^{2}	4.4260×10^{2}	-1.3376×10^{3}	1	1	6.0382×10^{1}	3.1851×10^{2}	5.7344×10^{2}	-1.9714×10^{2}
	2	6.1370×10^{3}	1.8041×10^{3}	6.8924×10^{3}	7.4361×10^{3}		2	-1.4459×10^{3}	-2.2502×10^{3}	-7.6421×10^{2}	8.6739×10^{2}
	3	-1.9212×10^{4}	-7.0660×10^{3}	-2.4498×10^{4}	-2.3730×10^{4}		3	6.1445×10^{3}	6.4450×10^{3}	-4.8194×10^{3}	-1.8693×10^{3}
	4	2.7068×10^{4}	8.4613×10^{3}	2.6786×10^{4}	2.7435×10^{4}		4	-7.6777×10^{3}	-6.8716×10^{3}	8.9350×10^{3}	1.9393×10^{3}
2	1	1.2787×10^{2}	-1.7090×10^{2}	-1.2681×10^{2}	-4.4791×10^{0}	2	1	-1.7614×10^{1}	-1.2134×10^{2}	-2.7928×10^{2}	-1.3483×10^{1}
	2	3.4026×10^{2}	-3.4948×10^{2}	-2.6843×10^{3}	3.0896×10^{2}		2	-7.6025×10^{1}	9.7328×10^{2}	7.2587×10^{2}	-2.2777×10^{0}
	3	-5.5783×10^{2}	2.2820×10^{3}	1.0265×10^{4}	-5.0206×10^{2}		3	4.2398×10^{2}	-3.0495×10^{3}	7.8740×10^{2}	6.7880×10^{1}
	4	5.0968×10^{2}	-2.9904×10^{3}	-1.1729×10^{4}	5.5584×10^{2}		4	-4.3262×10^{2}	3.3912×10^{3}	-2.5384×10^{3}	-2.0636×10^{1}
3	1	7.7706×10^{0}	-3.2669×10^{0}	-3.8706×10^{0}	4.9373×10^{-1}	3	1	-1.3294×10^{0}	-8.7101×10^{-1}	-2.0554×10^{0}	-6.0189×10^{-1}
	2	-2.2237×10^{0}	5.6413×10^{-1}	4.2270×10^{0}	-1.4159×10^{-2}		2	5.7954×10^{0}	7.4896×10^{0}	2.6510×10^{1}	3.7648×10^{0}
	3	1.0239×10^{1}	-2.3471×10^{0}	-4.0657×10^{0}	-4.2666×10^{-1}		3	-2.4358×10^{1}	-2.7404×10^{1}	-1.1789×10^{2}	-1.4110×10^{1}
	4	-1.2526×10^{1}	4.5049×10^{0}	-3.1396×10^{0}	8.8393×10^{-1}		4	3.9503×10^{1}	3.4409×10^{1}	1.5199×10^{2}	1.9464×10^{1}

TABLE V. Same as Table III, but at $E/A = 100$ MeV.

		Real part						Imaginary part			
k	i	$S = 0, T = 0$	$S = 0, T = 1$	$S = 1, T = 0$	$S = 1, T = 1$	k	i	$S = 0, T = 0$	$S = 0, T = 1$	$S = 1, T = 0$	$S = 1, T = 1$
1	1	3.2053×10^{1}	4.4868×10^{2}	4.7888×10^{2}	-1.1297×10^{3}	1	1	6.1620×10^{1}	2.8122×10^{2}	4.7208×10^{2}	-2.1982×10^{2}
	2	4.3230×10^{3}	1.8732×10^{3}	5.9566×10^{3}	5.5494×10^{3}		2	-1.5668×10^{3}	-1.7302×10^{3}	2.3175×10^{2}	9.9700×10^{2}
	3	-1.1847×10^{4}	-7.0318×10^{3}	-1.9863×10^{4}	-1.6704×10^{4}		3	6.7545×10^{3}	4.2846×10^{3}	-7.4272×10^{3}	-2.1954×10^{3}
	4	1.7097×10^{4}	8.2038×10^{3}	2.0560×10^{4}	1.8766×10^{4}		4	-8.6187×10^{3}	-4.0798×10^{3}	1.1211×10^{4}	2.1723×10^{3}
2	1	1.2794×10^{2}	-1.5914×10^{2}	-1.3513×10^{2}	-1.5087×10^{0}	2	1	-2.1709×10^{1}	-1.0283×10^{2}	-2.2915×10^{2}	-1.6490×10^{1}
	2	3.6062×10^{2}	-3.9108×10^{2}	-2.2288×10^{3}	2.9642×10^{2}		2	-7.5404×10^{1}	7.2610×10^{2}	2.5074×10^{2}	7.7433×10^{0}
	3	-6.1435×10^{2}	2.2983×10^{3}	7.9311×10^{3}	-4.5366×10^{2}		3	4.6670×10^{2}	-2.0365×10^{3}	2.0514×10^{3}	4.7968×10^{1}
	4	5.4031×10^{2}	-2.9053×10^{3}	-8.5569×10^{3}	4.8287×10^{2}		4	-5.2341×10^{2}	2.0912×10^{3}	-3.6586×10^{3}	-1.3948×10^{1}
3	1	7.6559×10^{0}	-3.3863×10^{0}	-4.2790×10^{0}	5.0570×10^{-1}	3	1	-1.6646×10^{0}	-6.2945×10^{-1}	-2.2298×10^{0}	-7.2930×10^{-1}
	2	-1.0584×10^{0}	9.9384×10^{-1}	7.7977×10^{0}	-1.3693×10^{-1}		2	9.2312×10^{0}	5.0022×10^{0}	2.9338×10^{1}	5.4849×10^{0}
	3	5.9068×10^{0}	-3.8375×10^{0}	-1.6524×10^{1}	-1.4793×10^{-1}		3	-3.9484×10^{1}	-1.8818×10^{1}	-1.2418×10^{2}	-2.1953×10^{1}
	4	-7.1020×10^{0}	6.6097×10^{0}	1.1422×10^{1}	6.9869×10^{-1}		4	5.8976×10^{1}	2.4674×10^{1}	1.5254×10^{2}	2.9740×10^{1}

TABLE VI. Same as Table III, but at $E/A = 120$ MeV.

		Real part						Imaginary part			
k	i	$S = 0, T = 0$	$S = 0, T = 1$	$S = 1, T = 0$	$S = 1, T = 1$	k	i	$S = 0, T = 0$	$S = 0, T = 1$	$S = 1, T = 0$	$S = 1, T = 1$
1	1	8.9200×10^{1}	4.4812×10^{2}	5.1434×10^{2}	-9.6317×10^{2}	1	1	3.3134×10^{1}	2.5387×10^{2}	4.1206×10^{2}	-2.4458×10^{2}
	2	3.0551×10^{3}	1.8264×10^{3}	5.3210×10^{3}	4.1856×10^{3}		2	-1.2390×10^{3}	-1.4244×10^{3}	5.7272×10^{2}	1.2066×10^{3}
	3	-7.0027×10^{3}	-6.6991×10^{3}	-1.7024×10^{4}	-1.1835×10^{4}		3	5.3789×10^{3}	3.1459×10^{3}	-7.4181×10^{3}	-2.9233×10^{3}
	4	1.0702×10^{4}	7.6838×10^{3}	1.6936×10^{4}	1.2888×10^{4}		4	-6.9036×10^{3}	-2.6918×10^{3}	1.0309×10^{4}	2.9700×10^{3}
2	1	1.2891×10^{2}	-1.5394×10^{2}	-1.4281×10^{2}	1.9398×10^{0}	2	1	-2.6833×10^{1}	-8.9803×10^{1}	-2.0186×10^{2}	-1.9615×10^{1}
	2	3.7360×10^{2}	-3.7886×10^{2}	-1.9263×10^{3}	2.7978×10^{2}		2	-5.9506×10^{1}	5.8082×10^{2}	1.0139×10^{2}	1.9039×10^{1}
	3	-6.4694×10^{2}	2.1551×10^{3}	6.5092×10^{3}	-3.9022×10^{2}		3	4.4994×10^{2}	-1.4977×10^{3}	2.0510×10^{3}	2.7654×10^{1}
	4	5.5140×10^{2}	-2.6569×10^{3}	-6.7134×10^{3}	3.9441×10^{2}		4	-5.4058×10^{2}	1.4360×10^{3}	-3.2634×10^{3}	-9.9338×10^{0}
3	1	7.5776×10^{0}	-3.5410×10^{0}	-4.6448×10^{0}	5.1860×10^{-1}	3	1	-1.7900×10^{0}	-4.4352×10^{-1}	-1.9983×10^{0}	-7.4973×10^{-1}
	2	-3.8337×10^{-1}	1.4715×10^{0}	1.0995×10^{1}	-3.2792×10^{-1}		2	1.0448×10^{1}	2.5323×10^{0}	2.3152×10^{1}	6.1899×10^{0}
	3	3.7599×10^{0}	-4.0067×10^{0}	-2.6400×10^{1}	4.7192×10^{-1}		3	-4.6282×10^{1}	-8.8789×10^{0}	-8.7674×10^{1}	-2.6350×10^{1}
	4	-4.6186×10^{0}	5.3951×10^{0}	2.0974×10^{1}	4.9920×10^{-2}		4	6.8576×10^{1}	1.2318×10^{1}	9.6875×10^{1}	3.6216×10^{1}

TABLE VII. Same as Table III, but at $E/A = 140$ MeV.

		Real part						Imaginary part			
k	i	$S = 0, T = 0$	$S = 0, T = 1$	$S = 1, T = 0$	$S = 1, T = 1$	k	i	$S = 0, T = 0$	$S = 0, T = 1$	$S = 1, T = 0$	$S = 1, T = 1$
	1	1.2446×10^{2}	4.5670×10^{2}	5.5018×10^{2}	-8.2833×10^{2}		1	-4.1791×10^{1}	2.3316×10^{2}	3.7274×10^{2}	-2.8366×10^{2}
1	2	2.2073×10^{3}	1.7175×10^{3}	4.8368×10^{3}	3.1804×10^{3}	1	2	-8.7335×10^{1}	-1.2353×10^{3}	6.5045×10^{2}	1.7393×10^{3}
	3	-3.9962×10^{3}	-6.1993×10^{3}	-1.5067×10^{4}	-8.3640×10^{3}		3	3.7563×10^{1}	2.5105×10^{3}	-6.6178×10^{3}	-5.2988×10^{3}
	4	6.8206×10^{3}	6.9933×10^{3}	1.4562×10^{4}	8.7593×10^{3}		4	3.6187×10^{2}	-1.9586×10^{3}	8.6903×10^{3}	6.1298×10^{3}
	1	1.3068×10^{2}	-1.5262×10^{2}	-1.5077×10^{2}	5.6983×10^{0}		1	-3.7557×10^{1}	-8.0215×10^{1}	-1.8509×10^{2}	-2.5052×10^{1}
2	2	3.7862×10^{2}	-3.4156×10^{2}	-1.7025×10^{3}	2.6065×10^{2}	2	2	4.7436×10^{1}	4.8902×10^{2}	6.9390×10^{1}	6.8913×10^{1}
	3	-6.5128×10^{2}	1.9539×10^{3}	5.5423×10^{3}	-3.1843×10^{2}		3	1.5623×10^{1}	-1.1868×10^{3}	1.7202×10^{3}	-1.7105×10^{2}
	4	5.3368×10^{2}	-2.3646×10^{3}	-5.5161×10^{3}	2.9853×10^{2}		4	1.1798×10^{1}	1.0765×10^{3}	-2.5876×10^{3}	2.3882×10^{2}
	1	7.5239×10^{0}	-3.7292×10^{0}	-4.9501×10^{0}	5.2820×10^{-1}		1	-1.2913×10^{0}	-3.1480×10^{-1}	-1.7630×10^{0}	-4.7474×10^{-1}
3	2	5.8283×10^{-2}	2.4930×10^{0}	1.4157×10^{1}	-5.4776×10^{-1}	3	2	2.0851×10^{0}	7.6714×10^{-1}	1.6885×10^{1}	2.3662×10^{0}
	3	2.4003×10^{0}	-7.2679×10^{0}	-3.7812×10^{1}	1.2891×10^{0}		3	-9.1816×10^{0}	-2.0319×10^{0}	-5.4412×10^{1}	-1.0065×10^{1}
	4	-2.9840×10^{0}	9.1576×10^{0}	3.4016×10^{1}	-8.8204×10^{-1}		4	1.8450×10^{1}	4.1791×10^{0}	5.0356×10^{1}	1.4604×10^{1}

[1] F. Coester, S. Cohen, B. D. Day, and C. M. Vincent, Phys. Rev. C **1**, 769 (1970).
[2] I. E. Lagaris and V. R. Pandharipande, Nucl. Phys. **A359**, 349 (1981).
[3] R. B. Wiringa, V. Fiks, and A. Fabrocini, Phys. Rev. C **38**, 1010 (1988).
[4] M. Baldo, I. Bombaci, and G. F. Burgio, Astron. Astrophys. **328**, 274 (1997).
[5] A. Lejeune, U. Lombardo, and W. Zuo, Phys. Lett. **B477**, 45 (2000).
[6] T. Furumoto, Y. Sakuragi, and Y. Yamamoto, Phys. Rev. C **79**, 011601 (2009).
[7] T. Furumoto, Y. Sakuragi, and Y. Yamamoto, Phys. Rev. C **78**, 044610 (2008).
[8] T. A. Rijken, Phys. Rev. C **73**, 044007 (2006).
[9] T. A. Rijken and Y. Yamamoto, Phys. Rev. C **73**, 044008 (2006).
[10] J. Fujita and H. Miyazawa, Prog. Theor. Phys. **17**, 360 (1957).
[11] D. T. Khoa, W. von Oertzen, and H. G. Bohlen, Phys. Rev. C **49**, 1652 (1994).
[12] D. T. Khoa, G. R. Satchler, and W. von Oertzen, Phys. Rev. C **56**, 954 (1997).
[13] G. Bertsch, J. Borysowicz, H. McManaus, and W. G. Love, Nucl. Phys. **A284**, 399 (1977).
[14] T. Kasahara, Y. Akaishi, and H. Tanaka, Prog. Theor. Phys. Suppl. **56**, 96 (1974).
[15] B. Sinha, Phys. Rep. **20**, 1 (1975).
[16] B. Sinha and S. A. Moszkowski, Phys. Lett. **B81**, 289 (1979).
[17] J. W. Negele and D. M. Vautherin, Phys. Rev. C **5**, 1472 (1972).
[18] X. Campi and A. Bouyssy, Phys. Lett. **B73**, 263 (1978).
[19] D. T. Khoa, Phys. Rev. C **63**, 034007 (2001).
[20] S. Nagata, M. Kamimura, and N. Yamaguchi, Prog. Theor. Phys. **73**, 512 (1985).
[21] M. Katsuma, Y. Sakuragi, S. Okabe, and Y. Kondo, Prog. Theor. Phys. **107**, 377 (2002).
[22] G. R. Satchler and W. G. Love, Phys. Rep. **55**, 183 (1979).
[23] F. Duggan, M. Lassaut, F. Michel, and N. V. Mau, Nucl. Phys. **A355**, 141 (1981).
[24] F. Carstoiu and M. Lassau, Nucl. Phys. **A597**, 269 (1996).
[25] T. Furumoto and Y. Sakuragi, Phys. Rev. C **74**, 034606 (2006).
[26] S. Okabe, in *Tours Symposium on Nuclear Physics II*, edited by H. Utsunomiya *et al.* (World Scientific, Singapore, 1995), p. 112.
[27] H. DeVries, C. W. DeJager, and C. DeVries, At. Data Nucl. Data Tables **36**, 495 (1987).
[28] L. R. B. Elton, *Nuclear Size* (Oxford University, Oxford, 1961).
[29] Y. Kondō, F. Michel, and G. Reidemeister, Phys. Lett. **B242**, 340 (1990).
[30] Y. Kondō, Y. Sugiyama, Y. Tomita, Y. Yamanouchi, H. Ikezoe, K. Ideno, S. Hamada, T. Sugimitsu, M. Hijiya, and H. Fujita, Phys. Lett. **B365**, 17 (1996).
[31] M. E. Brandan and G. R. Satchler, Phys. Rep. **285**, 143 (1997), and references therein.
[32] N. Yamaguchi, S. Nagata, and T. Matsuda, Prog. Theor. Phys. **70**, 459 (1983).
[33] F. Nuoffer *et al.*, Nuovo Cimento A **111**, 971 (1998).
[34] D. T. Khoa, W. von Oertzen, H. G. Bohlen, and S. Ohkubo, J. Phys. G: Nucl. Part. Phys. **34**, R111 (2007).
[35] P. Roussel-Chomaz, N. Alamanos, F. Auger, J. Barrette, B. Berthier, B. Fernandez, and L. Papineau, Nucl. Phys. **A477**, 345 (1988).
[36] T. Ichimura *et al.*, Nucl. Phys. **A569**, 287 (1994).
[37] K. Schwarz *et al.*, Eur. Phys. J. A **7**, 367 (2000).
[38] E. Stiliaris, H. G. Bohlen, P. Fröbrich, B. Gebauer, D. Kolbert, W. von Oertzen, M. Wilpert, and T. Wilpert, Phys. Lett. **B223**, 291 (1989).
[39] H. G. Bohlen *et al.*, Z. Phys. A **346**, 189 (1993).
[40] Y. Iseri, computer code ALPS (unpublished).
[41] T. Izumoto, S. Krewald, and A. Faessler, Nucl. Phys. **A341**, 319 (1980).
[42] T. Izumoto, S. Krewald, and A. Faessler, Nucl. Phys. **A357**, 471 (1981).
[43] T. Izumoto, S. Krewald, and A. Faessler, Nucl. Phys. **A359**, 509 (1981).